Cascade *L*-shell soft-x-ray emission as incident x-ray photons are tuned across the 1*s* ionization threshold

D. Sokaras,[1] A. G. Kochur,[2] M. Müller,[3] M. Kolbe,[3] B. Beckhoff,[3] M. Mantler,[4] Ch. Zarkadas,[1,5] M. Andrianis,[1]
A. Lagoyannis,[1] and A. G. Karydas[1,6]

[1]*Institute of Nuclear Physics, N.C.S.R. "Demokritos," Aghia Paraskevi, GR-15310, Athens, Greece*
[2]*Rostov State University of Transport Communication, 344038, Rostov-na-Donu, Russia*
[3]*Physikalisch-Technische Bundesanstalt, Abbestrasse 2-12, D-10587, Berlin, Germany*
[4]*Technische Universität Wien, A-1040, Vienna, Austria*
[5]*PANalytical B.V., 7600 AA Almelo, The Netherlands*
[6]*Nuclear Spectrometry and Applications Laboratory, International Atomic Energy Agency (IAEA), A-2444, Seibersdorf, Austria*

The cascade *L*-shell x-ray emission as an incident polarized and unpolarized monochromatic radiation overpass the 1*s* ionization threshold is investigated for the metallic Fe by means of moderate resolution, quantitative x-ray spectrometry. A full *ab initio* theoretical investigation of the *L*-shell x-ray emission processes is performed based on a detailed straightforward construction of the cascade decay trees within the Pauli-Fock approximation. The agreement obtained between experiments and the presented theory is indicated and discussed with respect to the accuracy of advanced atomic models as well as its significance for the characterization capabilities of x-ray fluorescence (XRF) analysis.

I. INTRODUCTION

A single photoionization event produces a short-lived atomic inner-shell-vacancy state. This excitation decays very fast (∼fs) through cascades of electronic transitions, until an ionic ground state is finally reached [1]. Each transition within the cascade is accompanied by an emission of either a photon (radiative transitions) or an electron (Auger and Coster-Kronig transitions). For core-level initial vacancies, the cascades can be very complex having up to millions of branches; thus their complete reliable theoretical description turns to be a rather sophisticated procedure.

The cascade decay of an inner-shell vacancy is a fundamental atomic phenomenon which should be considered in all the processes related to inner-shell vacancies. In x-ray spectroscopy, cascade decay manifests itself in the emission from less-deep shells when an initial vacancy is previously created in a deeper shell. In this case, the so-called cascade x-ray emission occurs [i.e., the x-ray emission from a shell where a vacancy (or vacancies) is created by the cascade decay processes and not directly as by photoionization or a charged-particle impact]. Although the cascade decays of inner-shell vacancy states, or vacancy cascades, have been being studied since the 1960s, the studies devoted to the cascade emission spectra are scarce [2–8].

In these terms, the development and the assessment of advanced theoretical models that have the potential to describe in a quantitatively reliable manner the high complexity fundamental atomic processes (i.e., the cascade relaxation) can be of great interest for the atomic physics field of research toward achieving an extensive understanding. Further on, the accurate study of the cascade x-ray emission through the theoretical description of atomic relaxation mechanisms,

besides having a profound interest in atomic physics, can also be of great importance in the applied physics research. X-ray fluorescence (XRF) spectroscopy can be considered as an advanced analytical method providing quantitative information on homogeneous, stratified, or even depth gradient materials in a wide field of applications [9]. The quantitative XRF analysis of unknown samples is usually based on the so-called fundamental parameters (FPs) method [10–12]. The FP method determines the unknown elemental concentrations or mass depositions through the iterative reconstruction of the detected x-ray fluorescence intensities, accounting for all the atomic processes contributing to the x-ray fluorescence as well as the given experimental setup characteristics (through the calibration constants). Knowing well the instrumental parameters by means of appropriate calibration procedures, the quantification analysis accuracy is mainly hampered by the reliability and the uncertainties of the tabulated FPs. Nevertheless, inconsistencies within FPs can be partly compensated within the calibration procedure utilizing certified reference materials and standards. One step further, the so-called reference-free XRF analysis [13,14], based on absolutely calibrated experimental setups, has the unique advantage not to rely on any relative measurement involving calibration specimens and, thus tends to serve the emerging needs for the characterization and quality control of advanced technological materials for which appropriate standards do not exist. However, in this case, inconsistencies and uncertainties in the FPs data base directly affect the accuracy of the quantitative analysis supporting the need for an assessment of the theoretical predictions with respect to experimentally determined FP values.

Within the XRF analysis of bulk materials, besides the well-known x-ray fluorescence induced by the single photoionization process, a number of second-order processes may also contribute to the observed x-ray emission. Various processes that involve the surrounding atoms (apart from

---

*dsokaras@inp.demokritos.gr

the one initially ionized), like the secondary fluorescence enhancement or the photoelectron or Auger-electron- induced secondary ionization, have also been identified to contribute to the primary x-ray fluorescence [15–20]. On the other hand, intraatomic effects like the resonant Raman scattering [21–26] or the cascade x-ray emission [18] are also expected to contribute significantly to the detected x-ray intensities, especially when monochromatic excited XRF analysis is employed at synchrotron radiation facilities.

In the present work, we thoroughly investigate the *L*-shell soft-x-ray emission upon photoionization by monochromatic polarized and unpolarized x-ray radiation tuning the photon energy across the 1*s* ionization threshold. Advanced *ab initio* calculations are explicitly performed both for the direct and the cascade-produced *L* emission spectra, through the straightforward construction of the cascade decay trees developed within the Pauli-Fock approximation. The processes of single- and multielectron photoionizations are distinguished and individually considered. The secondary effects, mainly related to the ejected electrons inducing ionizations of neighboring atoms, are carefully evaluated by means of detailed Monte Carlo calculations. As a case study, the metallic Fe is selected exemplarily.

II. THEORY

A. Cascade-produced photon spectra

The cascade-emitted x-ray spectra are calculated based on a straightforward construction of the cascade de-excitation trees via the method described in detail elsewhere [27,28], therefore, only a brief description is given below. An initial inner-shell vacancy produced by photoionization is short lived and it can decay through radiative and/or radiationless transitions into a number of ionic states forming in this way the set of first-generation cascade ionic states. Some of these, in their turn, can decay further forming the second-generation states and so on until all the vacancies are in the outermost shells and can decay no further. Initial and intermediate ionic states are the branching points in a cascade de-excitation tree, while each cascade transition from a given branching point is a branch in this tree. Every branch in the de-excitation tree is characterized by the branching ratio, defined as

$$\chi\left(C_k^{(n)} \to C_m^{(n+1)}\right) = \frac{\Gamma\left(C_k^{(n)} \to C_m^{(n+1)}\right)}{\sum_m \Gamma\left(C_k^{(n)} \to C_m^{(n+1)}\right)}. \qquad (1)$$

Here $C_k^{(n)}$ is an ionic configuration which appeared after the nth decay step, $C_m^{(n+1)}$ is the set of the next-decay-step configurations reached from $C_k^{(n)}$, and $\Gamma(C_k^{(n)} \to C_m^{(n+1)})$ is the partial width (transition rate) of respective transition. The summation is performed over all the possible final states $C_m^{(n+1)}$ reached from the branching point $C_k^{(n)}$ considering all radiative and radiationless (Auger, Coster-Kronig) transitions being energetically allowed. The partial transition widths are calculated in the configuration-average approximation using the Pauli-Fock (PF) wave functions [29] while the transition energies are calculated as differences of the mean total energies of initial and final ionic configurations.

The multivacancy ionic configurations of the cascade often have very complex multiplet structures due to electrostatic and spin-orbital interactions. The multiplets of initial and final configurations of some low-energy transitions may overlap, so that some term-to-term transitions are forbidden energetically. On the other hand, some term-to-term transitions are sometimes allowed even if the center of gravity of final configuration is higher in energy than that of the initial one. To account for that, the configuration multiplets are simulated with Gaussian probability density distributions with variances calculated via the methods described in [30]. This enables the modification of the partial widths when accounting for the multiplet overlaps.

To calculate the cascade-produced photon spectra, the energy interval of interest was split into the channels of equal width (0.2 eV), the energy of each radiative transition in a cascade was analyzed, and the transition probability was accumulated in respective energy channel. The transition probabilities (P) are calculated according to

$$P\left(C_1 \to C_2\right) = P\left(C_1\right)\chi\left(C_1 \to C_2\right), \qquad (2)$$

where C_1 and C_2 are initial and final configurations of the transition, $P(C_1)$ is the probability for the emitting configuration C_1 to appear during the cascade development, and χ is the branching ratio as defined in Eq. (1). The probability $P(C_1)$ is a product of all consecutive branching ratios of the consecutive branches leading from the initial inner-vacancy state to the emitting configuration C_1.

The principal feature of the cascade-produced spectra is their complex multicomponent structure caused by the multitude of transitions from a variety of different multivacancy configurations [4,5]. This is illustrated in Fig. 1 where the calculated Fe-*L* emission spectrum in a cascade decay of the 1*s*-vacancy state is presented. Most prominent lines in Fig. 1 are assigned by naming the transition and the set of additional vacancies in whose presence the transition takes place (in parentheses). In fact, the actual structure of the cascade-produced spectra is even more complex. Indeed, each bar in Fig. 1 represent transitions between multivacancy configurations. Then both initial and final states of most of the transitions are complex multicomponent multiplets, and there exist in fact a great number of term-to term transitions with different energies. A thorough calculation of the multiplet structure of each cascade transition is a very complicated problem which was addressed only once so far [8] and it is certainly outside the scope of this paper.

B. Photoionization cross sections and cascade emission on photoionization

Photoionization of an atom normally produces a number of ionic states that consequently may produce (directly or through a cascade decay) the x-ray emission. The photoionization cross sections are then the crucial quantities needed to be known in order to calculate the distributions of the initial inner-shell-vacancy states at various incident photon energies. The cross section of single 1*s*, 2*s*, and 2*p* ionization are calculated for an isolated Fe atom in a relaxed-core (RC) approximation via the methods described in Refs. [31,32]. The first-order-term-accurate expressions for the 1*s*-, 2*s*-, and 2*p*-photoionization

cross sections in the length form, are

$$\sigma_{1s \rightarrow \epsilon p} = \frac{4}{3}\pi^2 \alpha a_0^2 E S_{1s}^2 \left[\langle 1s|r|\epsilon p_+ \rangle - \frac{\langle 1s|r|2p_+ \rangle \langle 2p|\epsilon p_+ \rangle}{\langle 2p|2p_+ \rangle} - \frac{\langle 1s|r|3p_+ \rangle \langle 3p|\epsilon p_+ \rangle}{\langle 3p|3p_+ \rangle} \right]^2, \quad (3)$$

$$\sigma_{2s \rightarrow \epsilon p} = \frac{4}{3}\pi^2 \alpha a_0^2 E S_{2s}^2 \left[\langle 2s|r|\epsilon p_+ \rangle - \frac{\langle 2s|r|2p_+ \rangle \langle 2p|\epsilon p_+ \rangle}{\langle 2p|2p_+ \rangle} - \frac{\langle 2s|r|3p_+ \rangle \langle 3p|\epsilon p_+ \rangle}{\langle 3p|3p_+ \rangle} \right]^2, \quad (4)$$

$$\sigma_{2p \rightarrow \epsilon s} = \frac{4}{3}\pi^2 \alpha a_0^2 E S_{2p}^2 \left[\langle 2p|r|\epsilon s_+ \rangle - \frac{\langle 2p|r|1s_+ \rangle \langle 1s|\epsilon s_+ \rangle}{\langle 1s|1s_+ \rangle} - \frac{\langle 2p|r|2s_+ \rangle \langle 2s|\epsilon s_+ \rangle}{\langle 2s|2s_+ \rangle} - \frac{\langle 2p|r|3s_+ \rangle \langle 3s|\epsilon s_+ \rangle}{\langle 3s|3s_+ \rangle} \right]^2, \quad (5)$$

$$\sigma_{2p \rightarrow \epsilon d} = \frac{8}{3}\pi^2 \alpha a_0^2 E S_{2p}^2 \left[0.4\langle 2p|r|\epsilon d_+ \rangle^2 + 0.6\left(\langle 2p|r|\epsilon d_+ \rangle - \frac{\langle 2p|r|3d_+ \rangle \langle 3d|\epsilon d_+ \rangle}{\langle 3d|3d_+ \rangle} \right)^2 \right]. \quad (6)$$

Here α is the fine structure constant, a_0 is the Bohr radius, E is the incident photon energy, and ϵ is the energy of the ejected photoelectron. All the $\langle nl|$ atomic orbitals are optimized in the ground-state configurations while the $|\{n,\epsilon\}_+\rangle$ orbitals are in respective single-vacancy configurations; this is indicated by the "+" subscript. The terms S_{nl} are the products of the overlap

FIG. 1. (Color online) Fe-*L* emission spectrum produced by a cascade decay of the $1s^{-1}$ state (up). Most of the components represent the transitions in the presence of additional vacancies (shown in parentheses). Calculated x-ray emission spectra upon multielectron ionizations ($1s^{-1}4s^{-1}$, $1s^{-1}3d^{-1}$, $1s^{-1}3p^{-1}$) are also presented as discussed in Sec. II B.

integrals between the same atomic orbitals not involved in a photoelectron transitions, that is,

$$S_{nl} = \prod_i \langle n_i l_i | n_i l_{i+} \rangle^{N_i - \delta(n_i l_i, nl)}, \quad (7)$$

where N_i are the occupation numbers in the ground-state configuration $n_i l_i^{N_i}$. As shown in [31,32] the expressions (3)–(6) are valid if the photoelectron wave functions $|\epsilon l_+\rangle$ are optimized being orthogonal to the same-symmetry lower-lying $|n_i l_+\rangle$ atomic orbitals of the core-ionized atom.

Upon $1s$ and $2s$ photoionization, according to dipole selection rules, photoelectrons can have only p symmetry. In the case of $2p$ ionization both s and d channels are allowed, then the $2p$ cross section is the sum of Eqs. (5) and (6). However, the d channel is dominating, contributing about 97% of the total $2p$-subshell cross section. The $2p$-subshell configuration-average photoionization cross section does not account for the spin-orbital split of the $2p^{-1}$ level. This can be introduced by splitting the total $2p$ cross sections σ_{2p} into $\sigma_{L_2} = \frac{1}{3}\sigma_{2p}$ and $\sigma_{L_3} = \frac{2}{3}\sigma_{2p}$ according to the statistical weights.

The ionization threshold energies are calculated in an isolated-atom approximation as differences of total PF energies of nl-ionized and ground-state configurations. The corresponding energies of the L_2 and L_3 thresholds are calculated using the spin-orbit constant (ζ_{2p}) obtained for the $2p^{-1}$ configuration: $E(L_2) = E_{PF}(2p^{-1}) - E_{PF}(0) + \zeta_{2p}$, $E(L_3) = E_{PF}(2p^{-1}) - E_{PF}(0) - 0.5\zeta_{2p}$. All the calculated threshold energies are presented in Table I and compared with the corresponding values given in the Elam *et al.* database [34] and previous theoretical studies [35,36]. One can see that the calculated values are systematically higher than the experimental ones. This is due to extra-atomic relaxation upon creation of an inner-shell vacancy in a solid, a phenomenon evidently absent in a free atom [33]. Within further study, the calculated cross sections are shifted to the experimental threshold positions.

The calculated photoionization cross sections for the K and L shells of the iron atom are presented in Fig. 2 and compared with the widely used cross sections by Scofield [39]. As seen from Fig. 2, the obtained cross sections (continuous lines) are systematically lower than those by Scofield. The
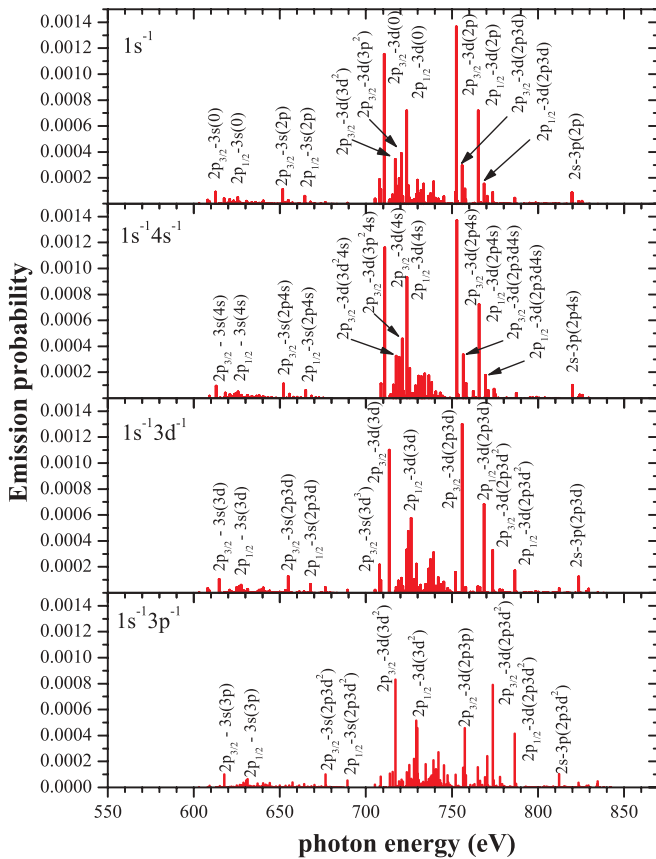
TABLE I. Calculated and experimental threshold energies (in eV) for Fe.

	Theory		
Shell	Present work	Previous work [33]	Experiment [34]
K	7134.3	7135[a][b]	7112.0[c]
L_1	861.9	863[a][b]	844.6[d]
L_2	735.5	736[a][b]	719.9[d]
L_3	722.6	722[a][b]	706.8[d]

[a]Reference [35].
[b]Reference [36].
[c]Reference [37].
[d]Reference [38].

reason for this discrepancy is in different approximations used in the calculations. In contrast to the relaxed-core (RC) approximation used here, a frozen-core (FC) approximation was employed by Scofield [39]. In FC approximation, upon photoionization all the atomic orbitals remain the same as in the ground state. This means that the overlap integrals present in Eqs. (3)–(6) are either unity (for the same orbitals) or zero (for different orbitals). Then, all the additional rearrangement terms in parentheses in Eqs. (3)–(6) disappear, and, most important, S_{nl}^2 terms [Eq. (7)] are now unity. However, in RC approximation these terms are $S_{1s}^2 = 0.7311$, $S_{2s}^2 = 0.7653$, and $S_{2p}^2 = 0.7601$, being the reason for lower cross sections in the RC approximation.

It should be noted that the S_{nl}^2 terms have a definite physical sense. The creation of an nl vacancy in an atom leads to the so-called shake processes (i.e., to additional excitations or ionizations of other, mostly outermost atomic subshells). In "sudden" approach [40], the squared overlap integral $\langle n_i l_i | n_i l_{i+}\rangle^2$ is the probability for the $n_i l_i$ electron to remain in its orbital upon the change of the potential caused by the appearance of the deep nl vacancy. Then, S_{nl}^2 defined in Eq. (7) is the probability that all the electrons of the atom except the ionized one will stay where they had been before

nl ionization. In other words, it is the probability of single nl ionization. Since the probability of any process to happen is unity, $1 - S_{nl}^2$ is then a combined probability of all multiple excitation or ionization processes accompanying nl ionization. The absence of the S_{nl}^2 terms in the cross section formulas of the FC approximations means that the FC cross sections contain implicitly all multiple ionization processes. In this way, far from the ionization thresholds FC cross sections normally compare well with the experiment [41].

In this work the shake processes are considered explicitly. Within the sudden approach [40] the relative probability of additional excitation or ionization of an $n_1 l_1$ subshell induced by a sudden vacancy creation in the nl subshell is

$$w(nl,n_1 l_1) = \frac{\sigma(nl^{-1} n_1 l_1^{-1})}{\sigma(nl^{-1})} = N_1(\langle n_1 l_1 | n_1 l_{1+}\rangle^{-2} - 1). \tag{8}$$

Here N_1 is the population of the $n_1 l_1$ subshell, while $\langle n_1 l_1 |$ and $| n_1 l_{1+}\rangle$ wave functions in the overlap integral are those optimized in the ground state and in the nl^{-1} configuration, respectively. Direct calculations of $\sigma(nl^{-1} n_1 l_1^{-1})$ cross sections near nl thresholds (see, e.g., [42]) showed that the sudden limit, expressed by Eq. (8), being independent of the exciting photon energy, is reached at incident photon energies above the nl threshold by about three times the $n_1 l_1$ ionization energy. This condition is fulfilled for the exciting energies considered within the present study (see Sec. III). The calculated relative shake probabilities of additional excitation or ionization of $3p$, $3d$, and $4s$ electrons upon $1s$, $2s$, and $2p$ ionization are presented in Table II and compared with the calculations of Mukoyama and Taniguchi [43] that are based on Hartree-Fock-Slater (HFS) wave functions. The relative probabilities of the shake processes compare well with those of Ref. [43] while the discrepancies seen are due mainly to different approximations used for the atomic wave functions in this work (PF) and in Ref. [43] (HFS) as discussed in detail elsewhere [44].

It should be noted that the probabilities of the shake processes given by Eq. (8) are combined probabilities of shake-up (SU) and shake-off (SO) processes. In SU process an outer-shell $n_1 l_1$ electron is excited to a higher-lying excited bound state, for example, $3d \to 4d$ while in SO processes the $n_1 l_1$ electron is ejected from the atom. The relative contributions from the SU and the SO processes to the total shake probability [Eq. (8)] can vary noticeably depending on
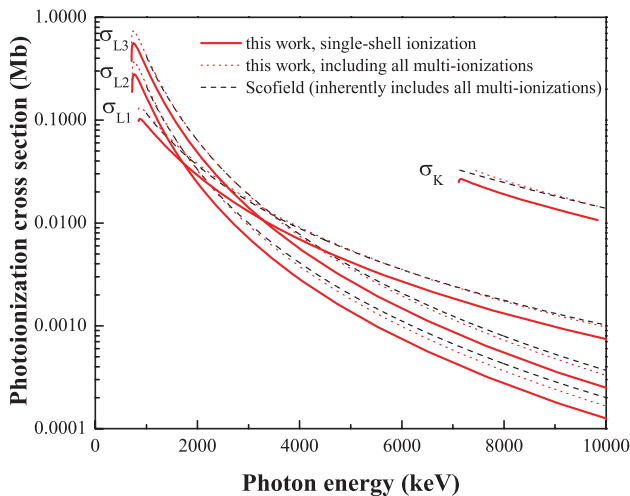

FIG. 2. (Color online) Photoionization cross section for free Fe atom. Single-shell and cumulative ionization cross sections based on relaxed core approximation (this work) are compared with frozen core calculations by Scofield [39] (dash lines).

TABLE II. Relative probabilities $w(nl,n_1 l_1)$ of shake processes involving the subshells $n_1 l_1$ upon creation of initial vacancy in the inner subshell nl. The results of Ref. [43] are shown in parentheses for comparison.

Initial	Additional vacancy $n_1 l_1$		
Vacancy nl	$3p$	$3d$	$4s$
$1s$	0.0410 (0.0480)	0.1132 (0.1321)	0.1446 (0.1451)
$2s$	0.0180 (0.0210)	0.1231 (0.1361)	0.1274 (0.1256)
$2p$	0.0192 (0.0240)	0.1218 (0.1386)	0.1327 (0.1276)

[a]The absolute probabilities of [43] were divided by respective probabilities of single ionizations S_{nl}^2.

the atom, the initial vacancy nl, and the affected subshell n_1l_1 [45]. A detailed analysis of the cascade decay of the $1s^{-1}4p^1$ excited state in Argon has shown that the excited electron in a bound Rydberg state affects the cascade little being mostly a spectator of rapid transitions involving the core electrons [46]. It is expected that this is a general situation, and the cascades originating from the SU states will not be very different from those starting from respective SO states. Therefore the total shake probabilities [Eq. (8)] are attributed to the formation of $nl^{-1}n_1l_1^{-1}$ states.

The consideration of multielectron ionization processes upon a photoabsorption ending up in a direct or a cascade x-ray emission, can be of great importance toward the exact calculation of the x-ray emission spectra. The presence of spectator vacancies can considerably affect the x-ray spectra as these satellite emission lines can vary from few up to several electron volts with respect to the diagram emission lines.

Let Spct(C) denote the x-ray spectrum emitted from a given ionic configuration C [for instance, Spct($1s^{-1}$), Spct($1s^{-1}4s^{-1}$), Spct($1s^{-1}3d^{-1}$), and Spct($1s^{-1}3p^{-1}$) are presented in Fig. 1]. Each component in Spct(C) is a dimensionless probability of a photon emission upon the decay of the configuration C. In this way the cumulative x-ray spectrum emitted after photoabsorption at a given exciting energy E_0 is

$$\text{Spct}(E_0) = \sum_C \sigma_C(E_0)\text{Spct}(C), \qquad (9)$$

where the summation is performed over the core ionic configurations C produced by photoionization [with cross section $\sigma_C(E_0)$]. For this study, the x-ray emission spectra for all the core ionic configurations $C = nl^{-1}$, $nl^{-1}3p^{-1}$, $nl^{-1}3d^{-1}$, $nl^{-1}4s^{-1}$, with $nl = 1s, 2s, 2p_{1/2}, 2p_{3/2}$ have been explicitly calculated. The components in Spct(E_0) are now the cross sections of lines emission. The emission spectra (Eq. (9)) can be very complex having multitudes of satellite components, especially if the energy is enough for the $1s$-shell ionization, and this can play an important role for the accurate calculation of self-attenuation of the emitted x rays within the sample.

It is introduced here a quantity $\omega_{nl}(C)$ which is a generalized fluorescence yield (GFY) (i.e., the fluorescence yield of the subshell nl for any given configuration C). Standard fluorescence yield is the probability of photon emission upon creation of a single vacancy in the subshell nl [i.e., in the present notation, $\omega_{nl} = \omega_{nl}(nl^{-1})$]. As discussed above, the generalized fluorescence yield $\omega_{nl}(C)$ can be noticeably different from ω_{nl} if the initial configuration C contains a vacancy (or vacancies) deeper than nl.

Evidently, the GFY can be split into the partial contributions coming from specific transitions,

$$\omega_{nl}(C) = \sum_i \omega_{nl \to n_i l_i}(C). \qquad (10)$$

Here the quantities $\omega_{nl \to n_i l_i}(C)$ are partial generalized fluorescence yields (PGFY) for a given ionic configuration C, $nl \to n_i l_i$ being the radiative transitions from the nl subshell which may happen during the decay of the configuration C.

It is worthwhile to introduce the PGFY associated with photoionization of a specific inner subshell n_0l_0, $\omega_{nl \to n_i l_i}^{n_0l_0}$. As discussed above, n_0l_0 photoionization produces not only

a singly ionized $n_0l_0^{-1}$ state, but also a number of doubly ionized $n_0l_0^{-1}n_1l_1^{-1}$ states with additional vacancies in outer n_1l_1 subshells. Each of the ionic states produced by n_0l_0 photoionization gives its contribution to the PGFY. These contributions are proportional to the probabilities of those states to appear in the n_0l_0-photoionization process. The PGFY associated with an n_0l_0 photoionization is then determined as

$$\omega_{nl \to n_i l_i}^{n_0l_0} = \left[1 + \sum_{n_1l_1} w(n_0l_0, n_1l_1) \right]^{-1} \left[\omega_{nl \to n_i l_i}\left(n_0l_0^{-1}\right) \right.$$
$$\left. + \sum_{n_1l_1} w(n_0l_0, n_1l_1)\omega_{nl \to n_i l_i}\left(n_0l_0^{-1}n_1l_1^{-1}\right) \right]. \quad (11)$$

Here $w(n_0l_0, n_1l_1)$ are relative probabilities of shake processes given in Table II. Partial generalized fluorescence yields Eq. (11) associated with $1s$, $2s$, $2p_{1/2}$, and $2p_{3/2}$ photoionization are presented in Table III.

The uncertainties incorporated in calculated atomic characteristics fall into two major categories. Firstly, there are inaccuracies coming from the numerical methods used in the calculation of atomic quantities. These can be controlled by setting the accuracy parameters for the iteration routines when calculating the wave functions. The atomic data reported in this section and in Sec. V are numerically accurate in the sense that all the digits are significant. Secondly, and most importantly, there are systematic inaccuracies coming from the approximations used; they can be estimated via comparison of the calculated data with the experiment. In the present configuration-average one-electron approximation based on the Pauli-Fock wave functions the following effects are neglected:

TABLE III. Partial generalized fluorescence yields associated with $1s$, $2s$, $2p_{1/2}$, and $2p_{3/2}$ photoionization of the Fe atom calculated with Eq. (11) taking double ionization processes into account. It should be noted that the x-ray emission energy for a given transition can vary noticeably depending on the number and the location of the spectator vacancies produced by the cascade relaxation processes (see Fig. 1).

Transition	Initial ionization			
	$1s$	$2s$	$2p_{1/2}$	$2p_{3/2}$
$1s$-$2p_{1/2}$	0.110	–	–	–
$1s$-$2p_{3/2}$	0.221	–	–	–
$1s$-$3p$	0.038	–	–	–
$2s$-$2p_{1/2}$	1.31×10^{-6}	4.34×10^{-6}	–	–
$2s$-$2p_{3/2}$	3.55×10^{-6}	1.16×10^{-5}	–	–
$2s - 3p$	1.86×10^{-4}	4.37×10^{-4}	–	–
$2p_{1/2}$-$3s$	2.88×10^{-4}	1.55×10^{-4}	4.52×10^{-4}	–
$2p_{1/2}$-$3d$	0.0029	0.0015	0.0055	–
$2p_{1/2}$-$4s$	1.87×10^{-5}	1.04×10^{-5}	3.01×10^{-5}	–
$2p_{3/2}$-$3s$	5.45×10^{-4}	3.36×10^{-4}	7.27×10^{-7}	4.26×10^{-4}
$2p_{3/2}$-$3d$	0.0056	0.0033	9.05×10^{-6}	0.0052
$2p_{3/2}$-$4s$	3.58×10^{-5}	2.25×10^{-5}	2.60×10^{-8}	2.86×10^{-5}
$3s$-$3p$	0.0068	0.0013	9.74×10^{-6}	9.66×10^{-6}
$3p$-$3d$	0.338	0.113	0.0065	0.0065
$3p$-$4s$	0.084	0.013	4.23×10^{-5}	4.23×10^{-5}

(i) Solid-state effects which may affect the probabilities of transitions with the participation of the outer atomic subshells, and absolute energies of ionic states.

(ii) Many-electron effects which in certain cases may affect emission spectra [47–50].

(iii) Multiplet splitting which affects the profiles of the emission spectra (note that the effect of multiplet splitting is effectively included when calculating the branching ratios).

Neglect of the solid-state effects is the most severe of the approximations adopted. As discussed in more detail in Sec. V, some decay channels, which are forbidden in an isolated-ion approximation, may open in solid state thus modifying the decay tree. As for the transition energies, they are expected to be affected since the solid-state extra-atomic relaxation effect is larger for the initial vacancy than for the final vacancy state of a transition. In the present work the calculated emission spectra were shifted by -5.9 eV in order for the calculated $L\alpha_1$ emission line to be in compliance with the corresponding experimental one [51] for the metallic iron. It should be noted that the shifts in emission spectra are less as compared with the shifts of the single levels (see ionization thresholds in Table I). This is because during transitions the extra-atomic relaxation—however different—is present both in initial and final states, and cancels out partially.

As for the many-electron and multiplet splitting effects, they are not expected to affect the cumulative cascade L spectra significantly. Indeed, these phenomena do not affect the integral intensities of the spectra, although sometimes affecting their profiles substantially: The intensity is split into a large number of components on wide energy intervals. This is of no importance in the present moderate energy resolution experiment registering the integral intensity of a bunch of transitions.

It should be noticed that similar approximations have been applied earlier in Ref. [7] in the description of the cumulative resonantly excited cascade $5d$-$4d$ emission from metallic lanthanum, as the exciting energy was scanned across the $3d$-$4f$ discrete excitation thresholds. A good agreement with the experiment obtained in Ref. [7] supports that the adopted theoretical approximations should be also applicable to the case of the L cascade emission in metallic iron.

C. Calculating Fe-*L* Yield

The total Fe-*L* detected intensity, $I_{\text{Fe}L}$, when a pure iron sample is irradiated with photons of energy E_0 and flux I_0, in the so-called parallel beam approximation, is given as

$$I_{\text{Fe}L} = I_0 \frac{\Delta\Omega}{4\pi} \sum_i P_i(E_0) \, M(E_o, E_i) \varepsilon(E_i) \frac{1}{\cos\theta_b}. \quad (12)$$

The sum runs over all the allowed transitions i [i.e., all the individual components of $\text{Spct}(E_0)$; Eq. (9)] with energy E_i and probability of emission P_i (cm^2 g^{-1}). $\Delta\Omega$ (sr) is the solid angle of detection confined by the aperture placed in front of the detector, ε is the detector efficiency at energy E_i, θ_b the angle of incidence with respect to the sample normal, and $M(E_o, E_s)$ (g cm^{-2}) stands for the absorption correction factor accounting for the incident and the fluorescence x-rays

self-attenuation within the iron sample defined according to its thickness as follows:

$$M(E_0, E_i) = \begin{cases} \frac{1 - e^{-\xi\mu_T}}{\mu_T}, & \text{intermediate thickness} \\ \frac{1}{\mu_T}, & \text{infinite thickness.} \end{cases} \quad (13)$$

ξ (g cm^{-2}) is the thickness of the sample and μ_T is given as

$$\mu_T = \frac{\mu(E_0)}{\cos\theta_b} + \frac{\mu(E_i)}{\cos\theta_d}, \quad (14)$$

whereas μ (cm^2 g^{-1}) stands for the iron sample mass attenuation coefficient at the corresponding energies and θ_d the emitted photons take-off angle with respect to the sample normal.

III. EXPERIMENT

The experimental study of the Fe-*L* cascade emission has been carried out by two individual series of measurements employing proton-induced x-ray beams and synchrotron radiation, respectively. The former series of experiments were realized at the novel proton-induced XRF chamber installed and operated at the 5.5-MV Tandem Van de Graaf accelerator laboratory of the Institute of Nuclear Physics at National Centre for Scientific Research, "Demokritos," Athens. The principle of the proton-induced XRF technique has been previously demonstrated and applied toward fundamental as well as analytical x-ray spectrometry studies over low-energy particle accelerator facilities [22–24,26]; the irradiation of a thick pure primary target by a few MeV high current proton beam forms a high intensity unpolarized x-ray source of selectable energy and high monochromaticity composed of the primary target characteristic radiation to be used for further x-ray-related studies. The two-level proton-induced XRF chamber hosts in the lower part up to six primary targets used for ion-beam irradiation selecting in this way the energy of the incident x-ray beam. In the upper level, a six-position rotatable sample holder hosts the samples considered for analysis (all incident and take-off angles are set to $45°$). The proton-induced x-ray beam is guided from the primary target to the sample position through a proper collimator whereas a filter can be inserted within its path in order to eliminate the backscattered protons and selectively absorb various spectral components of the incident x-ray beam. The chamber associates an energy dispersive ultrathin window (AP 1.7) Si(Li) spectrometer [full-width at half maximum (FWHM) 136 eV at 5.89 keV; Gresham Sirius] capable of detecting photons even below the C-$K\alpha$ fluorescence line. A double collimator system, placed in front of the detector window, confines the solid angle of detection to about 23 msr while the incorporated rare-earth magnets configuration prevents the photoelectrons or Auger electrons (up to $\sim$20 keV) to reach and deposit energy into the detector crystal. For monitoring the incident x-ray beam flux, the electrically isolated holder of the primary targets enables charge measurement of the impinging ion-beam current (that it is proportional related to the x-ray beam flux) whereas in addition, a p-i-n diode x-ray detector, placed at the lower level of the chamber, monitors during each measurement the primary proton-induced x-ray emission.

TABLE IV. Proton-induced x-ray beams: Primary targets, filters, incident proton, and x-ray beam energies.

Primary target	Proton beam (MeV)	Filter[a]	X-ray beam (keV)
Al	1.00	15 μm LDPE[b]	1.49
Si	1.00	15 μm LDPE[b]	1.74
NaCl	1.25	50 μm Kapton	2.65
Ti	1.75	10 μm Al & 43 μm Kapton	4.51
V	1.50	12.5 μm Ti & 25 μm LDPE[b] & 10 μm HDPE[c]	4.95
Cr	1.75	10 μmAl & 43 μm Kapton	5.41
Mn	1.50	20 μmAl & 25 μm Kapton	5.89
Fe	1.50	20 μm Mn	6.40
Co	1.50	23 μm Fe	6.93
Ni	1.50	17.5 μm Co	7.48
Cu	1.50	20 μm Ni	8.04
Zn	1.75	10 μm Cu & 13 μm Kapton	8.63

[a]Additionally a permanent filter, 9 μm of Kapton (DuPont), separates the two levels of the proton-induced XRF chamber.
[b]Low-density polyethylene.
[c]High-density polyethylene.

For the Fe-*L* cascade x-ray emission study, a thick, high-purity, freshly polished, metallic iron target was irradiated with incident x-ray beams of selectable photon energies across the Fe 1*s* shell ionization threshold. The various x-ray beams in the energy range 1.49–8.63 keV were formed by employing a large set of high-purity primary targets presented in Table IV. The properties that the primary targets had to fulfill are the high endurance over the high-current ($\sim\mu$A) proton beam irradiation conditions and a certain degree of electrical conductivity (the surface charging effects induced by the accumulation of the secondary electrons have to be eliminated, since they may lead to the emission of intense x-ray bremsstrahlung). As a proton-induced x-ray beam is based on the inner-shell ionizations, it consequently consists of a lot of characteristic x-ray lines emitted during the de-excitation of the target element. In this way, in order to produce highly monochromatic incident x-ray beams, proper filters were installed between the primary target and the iron sample that favor the strong attenuation of $K\beta$ with respect to $K\alpha$ radiation. These filters acted also as appropriate absorbers of the *L* or outer shells emission lines, and for the continuum radiation induced by the proton beam interactions with the primary target atoms. However, for certain primary targets (Ti, Cr, Mn), no such filters that favor the $K\beta$ attenuation were introduced, as the energy of their $K\beta$ line was lying energetically very close to the $K\alpha$ of the very next in the periodic table target element; in this way, its contribution within the total Fe-*L* emission could be subtracted extracting thus the net contribution of the $K\alpha$ line. For the lower atomic number primary targets utilized in the experiment (Al and Si), there is no filter available to produce a selective attenuation of the $K\beta$ line since the $K\alpha$ and $K\beta$ characteristic lines are relatively close with respect

to their energy; however, the incident x-ray beam can be considered rather monochromatic as the relative $K\alpha$ intensity is 97%–98%. For all the cases, proper polymer filters were also introduced in order to eliminate completely the flux of the backscattered protons in the direction of the incident x-ray beam. The proton beam energy was selected by assessing and combining together experimental and simulation data for each primary target in such a way as to optimize the Fe-*L* intensity versus background. The Fe-*L* intensity is obviously directly proportional to the available x-ray flux incident at the iron sample, accounting properly for the thick primary target x-ray emission yield and the absorption in the filters. The background below the Fe-*L* peak is mainly due to the Compton scattering of high-energy γ rays into the Si(Li) crystal induced by nuclear reactions between the proton beam and the primary target nuclei. Summarizing, the total x-ray flux on the sample position is estimated to be generally 10^6–10^7 photons s^{-1} for all the primary targets when a 1.0 μA proton beam is utilized.

As for the synchrotron radiation-based experiments, the monochromatic radiation provided by the four-crystal monochromator (FCM) beamline in the PTB laboratory [52] at the electron storage ring BESSY II was employed, optimized for metrology purposes. The beamline's leg ends up at a cylindrical ultrahigh vacuum chamber where an incident beam spot of 300 $\times$ 300 μm^2 with flux $\sim 10^{10}$ photons s^{-1} is delivered. The samples considered for irradiation are properly aligned in the center of the chamber forming a 45°/45° geometry, with respect to the sample normal, as the incident and the take-off angles are concerned. Furthermore, since the plane of detection coincides with the polarization plane of the incident radiation, the detectable contribution of Compton and Rayleigh scattered photons is minimized. The chamber associates an absolutely calibrated ultrathin window Si(Li) spectrometer (FWHM = 139 eV at 5.89 keV; Röntec) [53] capable of detecting efficiently photons down to the B-$K\alpha$ fluorescence line. The detector is placed behind a calibrated aperture defining precisely the solid angle of detection. More specifically for the purposes of the current study the aperture's diameter was set at 1.501 $\pm$ 0.004 mm and placed 59.4 $\pm$ 0.2 mm away from the sample center. Furthermore, a calibrated photodiode [54] placed behind the chamber and across the incident x-ray beam path, enables the radiant power to be determined absolutely.

For this study a high-purity metallic iron foil was employed and irradiated across an extended energy range (2.5–9.7 keV). In order to obtain the exact thickness of the foil (450 $\pm$ 14 nm), transmittance measurements were performed within the range of 4–10 keV incorporating the mass attenuation coefficients given in the Elam *et al.* database [34].

The tabulated mass attenuation coefficients include theoretically calculated photoabsorption and scattering (Rayleigh and Compton) interaction cross sections based on the free atom approximation. These values compared well with experimental ones, even for condensed matter, as long as the incident photon energy does not lie close to any shell or subshell absorption threshold. However, near the absorption edges, as well as at the low-energy x-ray regime (<2 keV), significant deviations are observed (XANES/EXAFS structures). For the present study, since the Fe-*L* emission lines lie very close to the Fe-*L* absorption edges, reliable mass attenuation coefficients
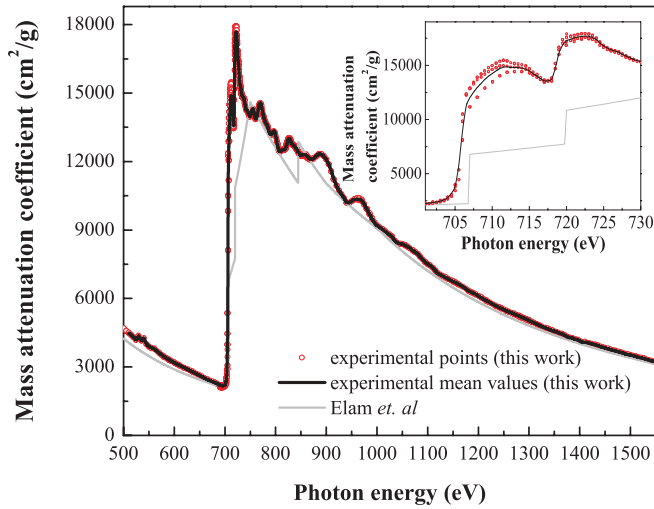
FIG. 3. (Color online) Experimental (this work) and theoretical [34] mass attenuation coefficients for metallic Fe in the energy region 500–1550 eV. The solid line represents the smoothed mean experimental values obtained by multiple transmittance energy scans.

FIG. 4. Electron impact ionization cross section for Fe-*L* sub-shells [59,60]. The Fe *K*-shell-based Auger spectra are also presented.

are of great importance in order to account properly for the self-attenuation in the Fe sample. For this purpose, the experimental mass attenuation coefficients were determined for the metallic Fe through transmittance measurements of monochromatic undulator radiation within the range of 500–1550 eV (with an energy step of 0.5–1 eV, the finest steps were selected across the Fe-*L* absorption thresholds) at the plane grating monochromator (PGM) beamline [55] (PTB laboratory at BESSY II), optimized also for metrology purposes. Employing an absolutely calibrated photodiode after the sample (the metallic Fe foil) and across the incident x-ray beam path, the transmitted radiant power was determined. The transmittance measurements were converted to experimental mass attenuation coefficients after accounting for the thickness of the Fe foil, measured, as discussed above, through another series of transmittance measurements at higher photon energies where the tabulated-theoretical mass attenuation coefficients are more reliable. The overall uncertainty for the determined mass attenuation coefficients within the energy range of 500–1550 eV is estimated to be within 5%−10%. These experimental values, obtained by multiple transmittance energy scans, as well as their mean smoothed value (continuous line) are plotted in Fig. 3 and compared to the tabulated ones by Elam *et al.* [34]. Apparently, very important deviations near the Fe-*L* absorption thresholds are observed, while the deviations are gradually eliminated at the higher photon energies.

IV. DATA ANALYSIS

The moderate resolution x-ray spectrometry studies provide the total detected Fe-*L* intensity for each of the employed incident x-ray beams. Common strategy in both sets of measurements is the absolute determination of the Fe-*L* intensities at every exciting x-ray beam energy per incident photon and steradian. At the same time, since metallic targets of infinite or intermediate thickness were employed during both experimental studies, all the secondary effects contributing to
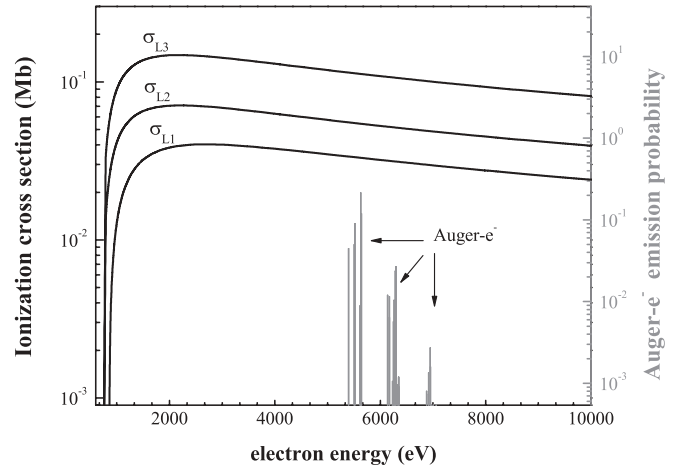
the Fe-*L* fluorescence intensity, have to be identified, evaluated, and subtracted before the detected Fe-*L* intensities could be compared to theoretical calculations.

The ejected photoelectrons, following the photoionization process, can be energetic enough to induce further inner-shell ionizations, enhancing in this way the Fe-*L* x-ray emission process. Furthermore, when the exciting x-ray beam energy overpasses the Fe 1*s* ionization threshold, the additional production of *KLL/KLM* Auger electrons (of ~5.6 keV)—with high probability—can also significantly contribute to the inner-shell ionization of the neighbor Fe atoms, see Fig. 4. The motion of energetic electrons inside a solid material follows a rather stochastic trajectory due to the very short mean free path of electron-electron interactions (elastic or inelastic). This complexity combined with the currently available computational power suggests that Monte Carlo–based calculations is the most efficient method for the study of electron-related processes within solids. For the evaluation of the photoelectron and Auger-electron induced Fe-*L* fluorescence, an in-house-developed Monte Carlo (MC) code was employed. Within the MC calculations, the crucial electron processes related to the total and differential elastic cross sections [56], the stopping power (that accounts for the energy loss due to inelastic processes) [57,58], as well as the inner-shell ionization cross sections [59,60] were incorporated. For the x-ray related processes, the Elam *et al* database [34] was adopted while the geometry (incident and take-off angle; sample thickness) for the simulations was selected in line with employed experimental setups.

When the Fe 1*s* ionization threshold for the incident x-ray beam energy is overpassed, the photoelectric absorption of the Fe *Kα* and *Kβ* characteristic lines within the sample can further induce the so-called secondary fluorescence enhancement of Fe-*L* line intensity. The influence of this effect has been extensively studied previously [15–17] both theoretically and experimentally validating the analytical formulation. The full Monte Carlo calculations mentioned above yielded the secondary fluorescence enhancement identical to the one calculated with the exact analytical formulas.

The determination of the absolute experimental Fe-*L* intensities is directly related to the $I_o \Delta \Omega \varepsilon(E_i)$ product [Eq. (12)].

For the synchrotron radiation setup, being optimized for metrology purposes, each of these factors are determined absolutely. For the proton-induced XRF setup, this product had to be found experimentally; the $I_o\Delta\Omega$ term was determined with a 4% precision through fluorescence measurements of pure monoelemental or well-characterized compound samples (down to fluorine $K\alpha = 677$ eV employing NaCl, Al, Si, CaF$_2$, Ti) for each of the proton-beam irradiated primary targets. The detector efficiency for the energies of the Fe-*L* lines (mostly 700 eV) and upward was calculated based on the experimentally measured transmission for the AP 1.7 ultrathin window (including the supporting silicon grid transmittance) provided by the manufacturer [61] and the nominal values for the nickel contact (120 Å) and the silicon dead layer (150 nm). The good precision of 4% in the determination of the $I_o\Delta\Omega$ term in the energy range covered by the fluorescence lines of the aforementioned calibration targets supports the model adopted for the detector efficiency calculation.

V. RESULTS AND DISCUSSION

The absolute cumulative Fe-*L* intensities for the proton-induced x rays and synchrotron radiation-based experiments are presented, with solid circles, in Figs. 5 and 5(b), respectively. The contributions from the secondary processes, (namely the photoelectron, Auger-electron, and secondary fluorescence enhancement) were calculated via the Monte Carlo technique and subtracted from the experimental data. They are shown with dotted lines in Figs. 5(a) and 5(b) (the secondary fluorescence contribution line for the thin metallic Fe foil lies well below the scale limits of Fig. 5(b)). The solid lines indicate the present work theoretical calculations for the cumulative Fe-*L* fluorescence intensity as a function of the incident photon energy [through Eq. (12)] incorporating the experimentally obtained mass attenuation coefficients for metallic Fe (Fig. 3). Both solid lines were multiplied with a factor of 0.83 and 0.81 in Figs. 5(a) and 5(b), respectively, in order to bring in compliance the theoretical prediction and experimental values.

The dot-dashed lines [Figs. 5(a) and 5(b)] indicate respective theoretical calculations based on previously reported fundamental parameters [34] and expressions [1] (i.e., multi-electron ionizations and satellite emission lines are excluded and tabulated mass attenuation coefficients are incorporated [34]). In order to account for the cascade enhancement to the Fe-*L* emission, the average number of primary L_i subshells vacancies (n_{KLi}) produced in the decay of one K vacancy were incorporated as deduced by Rao *et al.* [62] ($n_{KL1} = 0.21$, $n_{KL2} = 0.60$, $n_{KL3} = 0.66$). Finally, these dot-dashed lines were multiplied with the factor 0.47 and 0.41 in Figs. 5(a) and 5(b), respectively, in order to bring in compliance the theoretical prediction and experimental value at the lowest utilized exciting x-ray energy.

The much better agreement of the current work theoretical description with the experimental data, both in terms of the relative dependence of the cumulative Fe-*L*intensity as a function of the incident x-ray beam energy and regarding its absolute scale, relies (1) on the consideration of the exact x-ray emission spectra and (2) on the incorporation of the experimentally obtained mass attenuation coefficients for the
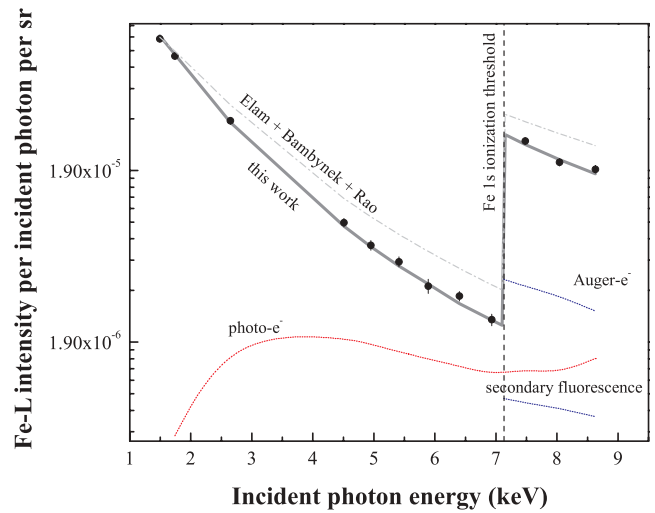
(a)
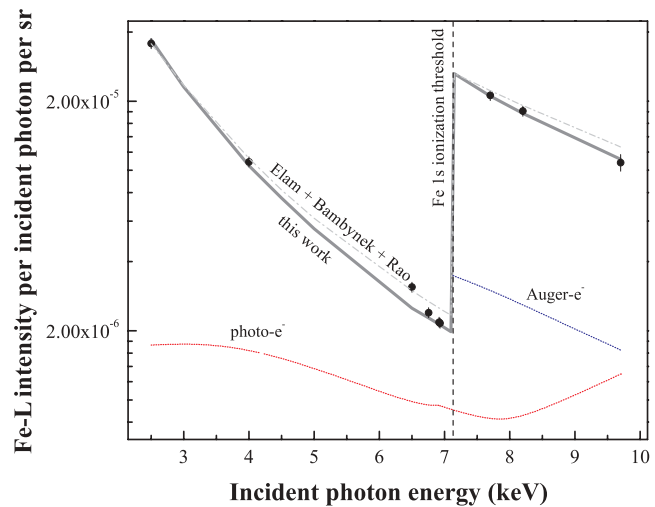
(b)

FIG. 5. (Color online) (a) Bulk metallic Fe (proton induced XRF, Demokritos). (b) 453 nm metallic Fe foil (FCM beamine, PTB, BESSY II). Experimental (solid circles) and theoretical cumulative Fe-*L* intensities based on the current work (solid line) and previous reported fundamental parameters (dot-dashed line). The contribution of the secondary effects to the Fe-*L* emission is also indicated (dotted lines).

metallic iron. Evidently, despite dealing with a moderate resolution x-ray spectrometry study, the detailed x-ray emission spectra is mandatory toward the accurate calculation of the Fe-*L* intensities as a function of the incident beam energy, both below and above the Fe 1*s* ionization threshold. As discussed in paragraph II B, the presence of spectator vacancies induce the emission of satellite lines varying from few up to several electron volts with respect to the diagram lines. Furthermore, since all these lines lie within the high-dynamics absorption regime of metallic Fe-*L* subshells, significant variations in the mass attenuation coefficient are observed, even for emission lines with sub-eV energy difference. However, when the self-attenuation effects become less important, the difference between the two theoretical calculations of the cumulative Fe-*L* intensity as a function of the incident x-ray beam energy

becomes less prominent. This becomes evident from the results for the thin metallic Fe foil utilized at the synchrotron radiation experiments [Fig. 5(b)], even though the difference in the absolute scale still remains. It is interesting to note that the discrepancy between the two theories increases as the incident photon energy varies from 1.5 to 7 keV [this is pronounced more in the bulk Fe case, see Fig. 5(a)]. It is evident that in the pre-*K*-edge region the slope of the Fe-*L* intensity against exciting photon energy is determined by *L*1-, *L*2- and *L*3-photoionization cross sections. It is seen from Fig. 2 that the relative contribution of the *L*1 ionization increases with the growth of the exciting photon energy. The characteristic x-ray lines emitted upon *L*1 photoionization are mainly emitted in the presence of an additional vacancy (created by an *L*1*L*2 or *L*1*L*3 Coster Kronig transition); they lie energetically above the *L*3 ionization threshold and are thus strongly absorbed. Only accurate calculation of the cascade-produced emission line energies allows one to account for this effect and to get an *L*-intensity dependence close to the experiment.

The cumulative uncertainties for the experimental absolute Fe-*L* intensities are estimated to be less than 10% in both sets of experimental measurements. These come from the individual uncertainties in the mass attenuation coefficients, in the thickness of the intermediate thickness Fe sample, in the calibration of the proton-induced XRF setup, and the databases for the electron-related processes considered in the Monte Carlo simulations. Therefore, the absolute difference among theory and experiment, being 17%–19%, clearly exceeds the

estimated experimental uncertainties which might be partially assigned to solid-state-related phenomena. Through the calculated partial generalized fluorescence yields (Table III), the fundamental atomic parameters for Fe, as obtained through the configuration-average Pauli-Fock approximation, have been extracted and compared with selected reported values in Table V. In general, a good agreement is observed with the respective theoretically deduced fundamental parameters which are mainly based on Dirac-Hartree-Slater [63,64] and Dirac-Fock [66,67] approximation. However, when compared to certain semiempirically extracted values [65] (shown in Table V in parentheses) some significant discrepancies are seen. It has been previously reported [65,68–70] that although the *L*2*L*3 Coster-Kronig process is energetically forbidden for the Fe free atoms (as well as for some neighbor transition metals with unfilled 3*d* shell), this transition is allowed in condensed matter due to solid-state effects. This discrepancy inevitably affects also the other competitive relaxation processes and thus the fluorescence yield of the *L*2 shell (ω_{L2}), too, which consequently also reduces the intensity of the Fe-*L* fluorescence lines.

Another important observation is related to the $Ll/L\alpha$ intensity ratio as it is deduced from the theoretical calculations versus the experimental findings. As depicted in Fig. 6, the theoretical emission spectra being convoluted with the response function of the Si(Li) spectrometer underestimates substantially the $Ll/L\alpha$ ratio when it is relatively compared to the corresponding experimental spectrum obtained from the pure bulk Fe sample, excited with photons of 1740 eV (Fig. 6). A similar behavior has also been shown recently by Müller *et al.* [71] for the metallic nickel case through a high-resolution x-ray spectrometry study; the experimentally obtained $Ll/L\alpha$ ratio found to exceed 20-30% various theoretical ratios. In the present work the $Ll/L\alpha$ ratio for metallic Fe is even much more pronounced and it is estimated to be ∼0.33 resulting thus in a difference of more than 300% with respect to theory. All the above indicate that condensed-matter-related effects are

TABLE V. Fundamental parameters for Fe as calculated in this work and compared with selected previously reported values.

	This work	Previous works
Fluorescence yields		
ω_K	0.369	0.351[a]
ω_{L1}	0.000 45	0.000 40[a]
ω_{L2}	0.005 94	0.0054[a] (0.0036)[b]
ω_{L3}	0.005 64	0.0059[a]
Coster-Kronig transitions		
f_{13}	0.65	0.68[a]
f_{12}	0.28	0.27[a]
f_{23}	0.00	0.00[a] (0.42)[b]
Relative intensities		
1s-2$p_{1/2}$ ($K\alpha_2$)	0.298	0.297[c]
1s-2$p_{3/2}$ ($K\alpha_1$)	0.599	0.581[c]
1s-3p ($K\beta$)	0.104	0.122[c]
2s-2$p_{1/2}$ (f'_{12})	0.010	–
2s-2$p_{3/2}$ (f'_{13})	0.026	0.021[d]
2s-3p ($L\beta_{2,3}$)	0.965	0.979[d]
2$p_{1/2}$-3s (Ln)	0.076	0.082[d]
2$p_{1/2}$-3d ($L\beta_1$)	0.919	0.910[d]
2$p_{1/2}$-4s	0.005	0.007[d]
2$p_{3/2}$-3s (Ll)	0.075	0.086[d]
2$p_{3/2}$-3d ($L\alpha_{1,2}$)	0.920	0.907[d]
2$p_{3/2}$-4s ($L\beta_6$)	0.005	0.008[d]

[a]References [63] and [64].
[b]Semiempirical corrections for condensed matter [65].
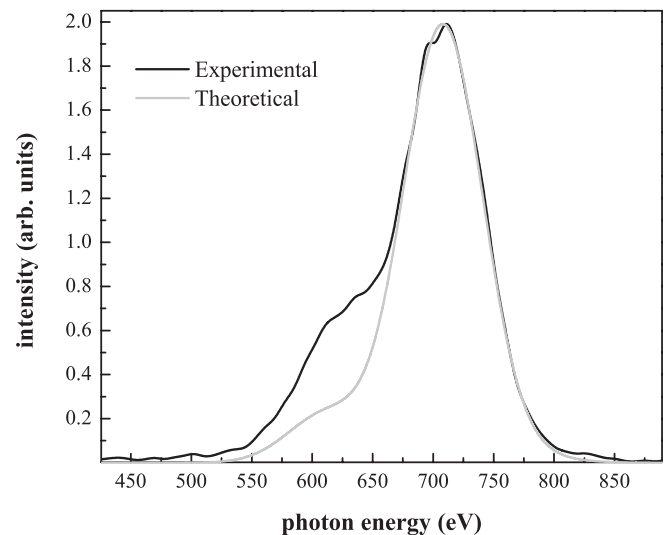[c]Reference [66].
[d]Reference [67].

FIG. 6. (Color online) Relative comparison of experimental and theoretical [convoluted with Si(Li) spectrometer response function] emission spectra, normalized at their maxima, when an incident x-ray beam of 1740 eV irradiates the bulk iron sample.

most probably responsible for these observed deviations, since they can affect considerably outermost-shell-related atomic processes which are not being described by theoretical models based on the free atom approximation.

VI. CONCLUSIONS

In this work, through moderate resolution x-ray spectrometry, the cumulative *L*-shell soft-x-ray emission of Fe was found to be independent from the polarization state of the incident radiation–within the experimental uncertainties–in accordance with the dipole approximation. The detailed *ab initio* theoretical approach, based on the direct construction of the cascade de-excitation trees within the Pauli-Fock approximation, showed that the exact calculation of the direct and the cascade x-ray emission spectra is mandatory for the accurate description of the absolute Fe-*L* x-ray emission intensity when the exciting radiation energy is scanned across the Fe 1*s* ionization threshold. Multielectron ionizations and cascade autoionization processes leading toward multivacancy states, induce the emission of satellite lines which in certain cases experience substantially different (higher) self-attenuation as compared to the diagram emission lines. In order to correctly calculate the self-attenuation for the *L*-shell soft x rays, experimental mass attenuation coefficients are found to be essential. Further on, secondary ionizations due to energetic electron motion can give considerable contribution to the emission and have to be appropriately accounted for. An isolated-atom approximation sets certain limitations regarding the description of specific inner-shell processes when compared to experimental observations in the metallic phase. The latter indicates the need for a complete overall *ab initio* theory incorporating core-electron processes and condensed matter or chemical environment effects, especially when open-shell-related processes are investigated. The overall insights presented here are also expected to improve considerably the reference-free x-ray fluorescence quantitative analysis applied for the characterization of advanced technological materials.

[1] W. Bambynek, B. Crasemann, R. W. Fink, H.-U. Freund, H. Mark, C. D. Swift, R. E. Price, and P. V. Rao, Rev. Mod. Phys. **44**, 716 (1972).

[2] E. T. Verkhovtseva, E. V. Gnatchenko, P. S. Pogrebnyak, and A. A. Tkachenko, J. Phys. B **19**, 2089 (1986).

[3] E. T. Verkhovtseva and P. S. Pogrebnjak, J. Phys. B **13**, 3535 (1980).

[4] A. G. Kochur, Ye. B. Mitkina, and V. L. Sukhorukov, J. Phys. B **31**, 5293 (1998).

[5] A. G. Kochur, V. L. Sukhorukov, and Ye. B. Mitkina, J. Phys. B **33**, 2949 (2000).

[6] G. Omar and Y. Hahn, Z. Phys. D **25**, 41 (1992).

[7] A. Moewes, R. G. Wilks, A. G. Kochur, and E. Z. Kurmaev, Phys. Rev. B **72**, 075129 (2005).

[8] A. G. Kochur, S. Brühl, I. D. Petrov, and Ye. B. Mitkina, Eur. Phys. J. Special Topics **169**, 51 (2009).

[9] M. West, A. T. Ellis, P. Kregsamer, P. J. Potts, C. Streli, C. Vanhoff, and P. Wobrauschek, J. Anal. At. Spectrom. **23**, 1409 (2008).

[10] M. Mantler, J. P. Willis, G. R. Lachance, B. A. R. Vrebos, K.-E. Mauser, N. Kawahara, R. M. Rousseau, and P. N. Brouwer, in *Handbook of Practical X-Ray Fluorescence Analysis*, edited by B. Beckhoff, B. Kanngiesser, N. Langhoff, R. Wedell, and H. Wolff (Springer, New York, 2006), pp. 309–410.

[11] R. M. Rousseau, X-Ray Spectrom. **13**, 115 (1984).

[12] R. M. Rousseau, X-Ray Spectrom. **13**, 121 (1984).

[13] B. Beckhoff, J. Anal. At. Spectrom. **23**, 845 (2008).

[14] B. Beckhoff, R. Fliegauf, M. Kolbe, M. Müller, J. Weser, and G. Ulm, Anal. Chem. **79**, 7873 (2007).

[15] D. K. G. de Boer, X-ray Spectrom. **19**, 145 (1990).

[16] M. Mantler, Anal. Chim. Acta **188**, 25 (1986).

[17] A. G. Karydas, X-ray Spectrom. **34**, 426 (2005).

[18] N. Kawahara, T. Shoji, T. Yamada, Y. Kataoka, B. Beckhoff, G. Ulm, and M. Mantler, Adv. X-ray Anal. **45**, 511 (2002).

[19] B. Beckhoff, M. Kolbe, O. Hahn, A. G. Karydas, Ch. Zarkadas, D. Sokaras, and M. Mantler, X-ray Spectrom. **37**, 462 (2008).

[20] A. Owens, B. Beckhoff, M. Kolbe, M. Krumrey, A. Mantero, M. Mantler, A. Peacock, M.-G. Pia, D. Pullan, U. G. Schneider, and G. Ulm, Anal. Chem. **80**, 8398 (2008).

[21] C. J. Sparks Jr., Phys. Rev. Lett. **33**, 262 (1974).

[22] A. G. Karydas, S. Galanopoulos, Ch. Zarkadas, T. Paradellis, and N. Kallithrakas-Kontos, J. Phys. Condens. Matter **14**, 12367 (2002).

[23] A. G. Karydas and Th. Paradellis, J. Phys. B **30**, 1893 (1997).

[24] Ch. Zarkadas, A. G. Karydas, M. Müller, and B. Beckhoff, Spectrochim. Acta, Part B **61**, 189 (2006).

[25] M. Mueller, B. Beckhoff, G. Ulm, and B. Kanngiesser, Phys. Rev. A **74**, 012702 (2006).

[26] D. Sokaras, M. Müller, M. Kolbe, B. Beckhoff, Ch. Zarkadas, and A. G. Karydas, Phys. Rev. A **81**, 012703 (2010).

[27] A. G. Kochur, A. I. Dudenko, V. L. Sukhorukov, and I. D. Petrov, J. Phys. B **27**, 1709 (1994).

[28] A. G. Kochur, V. L. Sukhorukov, A. I. Dudenko, and Ph. V. Demekhin, J. Phys. B **28**, 387 (1995).

[29] R. Kau, I. D. Petrov, V. L. Sukhorukov, and H. Hotop, Z. Phys. D **39**, 267 (1997).

[30] R. Karaziya, *Sums of Atomic Quantities and Mean Characteristics of Spectra* (Mokslas, Vilnius, 1991).

[31] V. L. Sukhorukov, V. F. Demekhin, V. V. Timoshevskaya, and S. V. Lavrentev, Opt. Spectrosc. (USSR) **47**, 407 (1979).

[32] V. L. Sukhorukov, V. F. Demekhin, V. A. Yavna, A. I. Dudenko, and V. V. Timoshevskaya, Opt. Spectrosc. (USSR) **55**, 229 (1983).

[33] D. A. Shirley, R. L. Martin, S. P. Kowalczyk, F. R. McFeely, and L. Ley, Phys. Rev. B **15**, 544 (1977).

[34] W. T. Elam, B. D. Ravel, and J. R. Sieber, Radiat. Phys. Chem. **63**, 121 (2002).

[35] K. Siegbahn *et al.*, Nova Acta R. Soc. Sci. Ups **20**, (1967).

[36] U. Gelius, Phys. Scr. **9**, 133 (1974).

[37] J. A. Bearden and A. F. Burr, Rev. Mod. Phys. **39**, 125 (1967).

[38] J. C. Fuggle and N. Martensson, J. Electron Spectrosc. Relat. Phenom. **21**, 275 (1980).

[39] J. H. Scofield, Lawrence Livermore Laboratory, Report No. UCRL-51326, 1973.

[40] V. P. Sachenko and V. F. Demekhin, Sov. Phys. JETP **22**, 532 (1966).

[41] H. Ebel, R. Svagera, M. F. Ebel, A. Shaltout, and J. H. Hubbell, X-ray Spectrum. **32**, 442 (2003).

[42] A. G. Kochur, A. M. Nadolinsky, and V. F. Demekhin, J. de Phys. Colloque C8 **47**, C8 (1986).

[43] T. Mukoyama and K. Taniguchi, Phys. Rev. A **36**, 693 (1987).

[44] A. G. Kochur and V. A. Popov, J. Phys. B **39**, 3335 (2006).

[45] A. G. Kochur and V. A. Popov, Radiat. Phys. Chem. **75**, 1525 (2006).

[46] A. G. Kochur, A. I. Dudenko, I. D. Petrov, and V. F. Demekhin, J. Electron Spectrosc. Relat. Phenom. **156**, 78 (2007).

[47] V. F. Demekhin, V. L. Sukhorukov, V. A. Yavna, S. A. Kulagina, S. A. Prosandeyev, and Yu. I. Bayrachny, Bull. Acad. Sci. USSR Phys. Ser. **40**, 28 (1976).

[48] V. L. Sukhorukov, S. A. Yavna, V. F. Demekhin, and B. M. Lagutin, Koordinatsionnaya Khimiya (USSR) **22**, 510 (1985).

[49] V. L. Sukhorukov, I. D. Petrov, V. F. Demekhin, and S. V. Lavrentiev, Izvesyiya Akademii Nauk USSR. Seriya Fizicheskaya **49**, 1463 (1985).

[50] V. L. Sukhorukov, I. D. Petrov, B. M. Lagutin, S. A. Yavna, and V. F. Demekhin, Koordinatsionnaya Khimiya (USSR) **12**, 205 (1986).

[51] R. D. Deslattes *et al.*, Rev. Mod. Phys. **75**, 35 (2003).

[52] B. Beckhoff, A. Gottwald, R. Klein, M. Krumrey, R. Müller, M. Richter, F. Scholze, R. Thornagel, and G. Ulm, Phys. Status Solidi B **246**, 1415 (2009).

[53] F. Scholze and M. Procop, X-Ray Spectrum. **30**, 69 (2001).

[54] A. Gottwald, U. Kroth, M. Krumrey, M. Richter, F. Scholze, and G. Ulm, Metrologia **43**, 125 (2006).

[55] F. Senf, U. Flechsig, F. Eggenstein, W. Gudat, R. Klein, H. Rabus, and G. Ulm, J. Synchrotron Radiat. **5**, 780 (1997).

[56] Z. Czyzewski, D. O. MacCallum, A. Romig, and D. C. Joy, J. Appl. Phys. **68**, 3066 (1990).

[57] J. M. Fernandez-Varea, R. Mayol, D. Liljequist, and F. Salvat, J. Phys. Condens. Matter **5**, 3593 (1993).

[58] A. Jablonski, S. Tanuma, and C. J. Powell, Surf. Interface Anal. **38**, 76 (2006).

[59] D. Bote, F. Salvat, A. Jablonski, and C. J. Powell, At. Data Nucl. Data Tables **95**, 871 (2009).

[60] D. Bote and F. Salvat, Phys. Rev. A **77**, 042701 (2008).

[61] P. Smith, e2v Scientific Instruments (private communication).

[62] P. Venugopala Rao, M. H. Chen, and B. Crasemann, Phys. Rev. A **5**, 997 (1972).

[63] M. H. Chen, B. Crasemann, and H. Mark, Phys. Rev. A **21**, 436 (1980).

[64] M. H. Chen, B. Crasemann, and H. Mark, Phys. Rev. A **24**, 177 (1981).

[65] M. O. Krause, J. Phys. Chem. Ref. Data **8**, 307 (1979).

[66] J. H. Scofield, Phys. Rev. A **9**, 1041 (1974).

[67] J. H. Scofield, Phys. Rev. A **10**, 1507 (1974).

[68] S. L. Sorensen, S. J. Schaphorst, S. B. Whitfield, B. Crasemann, and R. Carr, Phys. Rev. A **44**, 350 (1991).

[69] S. Iacobucci, F. Sirotti, M. Sacchi, and G. Stefani, J. Electron Spectrosc. Relat. Phenom. **123**, 397 (2002).

[70] M. O. Krause, C. W. Nestor, C. J. Sparks, and E. Ricci, Oak Ridge National Laboratory, Report No. ORNL-5399, 1978.

[71] M. Müller, B. Beckhoff, R. Fliegauf, and B. Kanngiesser, Phys. Rev. A **79**, 032503 (2009).